



The Pristine survey - XX: GTC follow-up observations of extremely metal-poor stars identified from Pristine and LAMOST

Anke Arentsen, David S. Aguado, Federico Sestito, González Jonay I. Hernández,
Nicolas F. Martin, Else Starkenburg, Pascale Jablonka, Zhen Yuan

► To cite this version:

Anke Arentsen, David S. Aguado, Federico Sestito, González Jonay I. Hernández, Nicolas F. Martin, et al.. The Pristine survey - XX: GTC follow-up observations of extremely metal-poor stars identified from Pristine and LAMOST. Monthly Notices of the Royal Astronomical Society, 2023, <10.1093/mnras/stad043>. <insu-03952792>

HAL Id: insu-03952792

<https://insu.hal.science/insu-03952792v1>

Submitted on 12 Jul 2023

HAL is a multi-disciplinary open access archive for the deposit and dissemination of scientific research documents, whether they are published or not. The documents may come from teaching and research institutions in France or abroad, or from public or private research centers.

L'archive ouverte pluridisciplinaire **HAL**, est destinée au dépôt et à la diffusion de documents scientifiques de niveau recherche, publiés ou non, émanant des établissements d'enseignement et de recherche français ou étrangers, des laboratoires publics ou privés.



HAL Authorization

The *Pristine* survey – XX. GTC follow-up observations of extremely metal-poor stars identified from *Pristine* and LAMOST

Anke Arentsen^{1,2,★}, David S. Aguado^{3,4}, Federico Sestito⁵, Jonay I. González Hernández^{6,7},
Nicolas F. Martin^{8,9}, Else Starkenburg⁹, Pascale Jablonka^{10,11} and Zhen Yuan^{10,2}

¹Institute of Astronomy, University of Cambridge, Madingley Road, Cambridge CB3 0HA, UK

²Observatoire Astronomique de Strasbourg, Université de Strasbourg, CNRS, UMR 7550, F-67000 Strasbourg, France

³Dipartimento di Fisica e Astronomia, Università degli Studi di Firenze, Via G. Sansone 1, I-50019 Sesto Fiorentino, Italy

⁴INAF – Osservatorio Astrofisico di Arcetri, Largo E. Fermi 5, I-50125 Firenze, Italy

⁵Department of Physics and Astronomy, University of Victoria, PO Box 3055, STN CSC, Victoria, BC V8W 3P6, Canada

⁶Instituto de Astrofísica de Canarias, E-38205 La Laguna, Tenerife, Spain

⁷Departamento de Astrofísica, Universidad de La Laguna, E-38206 La Laguna, Tenerife, Spain

⁸Max-Planck-Institut für Astronomie, Königstuhl 17, D-69117 Heidelberg, Germany

⁹Kapteyn Astronomical Institute, University of Groningen, Postbus 800, NL-9700 AV Groningen, the Netherlands

¹⁰Laboratoire d'astrophysique, École Polytechnique Fédérale de Lausanne (EPFL), Observatoire, CH-1290 Versoix, Switzerland

¹¹GEPI, Observatoire de Paris, Université PSL, CNRS, Place Jules Janssen, F-92195 Meudon, France

Accepted 2023 January 5. Received 2023 January 5; in original form 2022 November 3

ABSTRACT

Ultra-metal-poor stars ($[\text{Fe}/\text{H}] < -4.0$) are very rare, and finding them is a challenging task. Both narrow-band photometry and low-resolution spectroscopy have been useful tools for identifying candidates, and in this work, we combine both approaches. We cross-matched metallicity-sensitive photometry from the *Pristine* survey with the low-resolution spectroscopic Large Sky Area Multi-Object Fibre Spectroscopic Telescope (LAMOST) data base, and re-analysed all LAMOST spectra with $[\text{Fe}/\text{H}]_{\text{Pristine}} < -2.5$. We find that $\sim 1/3$ rd of this sample (selected without $[\text{Fe}/\text{H}]_{\text{Pristine}}$ quality cuts) also have spectroscopic $[\text{Fe}/\text{H}] < -2.5$. From this sample, containing many low signal-to-noise ratio (S/N) spectra, we selected 11 stars potentially having $[\text{Fe}/\text{H}] < -4.0$ or $[\text{Fe}/\text{H}] < -3.0$ with very high carbon abundances, and we performed higher S/N medium-resolution spectroscopic follow-up with the Optical System for Imaging and low Resolution Integrated Spectroscopy (OSIRIS) on the 10.4-m Gran Telescopio Canarias (GTC). We confirm their extremely low metallicities, with a mean of $[\text{Fe}/\text{H}] = -3.4$, and the most metal-poor star having $[\text{Fe}/\text{H}] = -3.8$. Three of these are clearly carbon-enhanced metal-poor (CEMP) stars with $+1.65 < [\text{C}/\text{Fe}] < +2.45$. The two most carbon-rich stars are either among the most metal-poor CEMP-s stars or the most carbon-rich CEMP-no stars known, the third is likely a CEMP-no star. We derived orbital properties for the OSIRIS sample and find that only one of our targets can be confidently associated with known substructures/accretion events, and that three out of four inner halo stars have prograde orbits. Large spectroscopic surveys may contain many hidden extremely and ultra-metal-poor stars, and adding additional information from e.g. photometry as in this work can uncover them more efficiently and confidently.

Key words: techniques: spectroscopic – stars: chemically peculiar – stars: Population II – Galaxy: halo.

1 INTRODUCTION

The most metal-poor stars still present in the Milky Way today are valuable portals to the early Universe and the *Pristine* environments these stars were born in. They are thought to have formed from material enriched by the first generation(s) of stars, and their chemical abundances can be used to constrain the properties of the stars that came before them. Additionally, the dynamical properties of the most metal-poor stars teach us about the early formation of the Milky Way. Much can be, and has been, learned from very/extremely/ultra-metal-poor stars with $[\text{Fe}/\text{H}] < -2.0$ (VMP)/ -3.0 (EMP)/ -4.0 (UMP)

(e.g. Beers & Christlieb 2005; Frebel & Norris 2015), although they are exceedingly rare.

The metal-poor halo has been found to be a melting pot of many accreted structures. It is populated by the remnants of the larger mergers that the Galaxy experienced across its history, such as Gaia-Sausage/Enceladus (GSE; e.g. Belokurov et al. 2018; Helmi et al. 2018), Sequoia (e.g. Barbá et al. 2019; Myeong et al. 2019), Thamnos (e.g. Koppelman et al. 2019), and Sagittarius (e.g. Ibata, Gilmore & Irwin 1994). The plethora of recently discovered stellar streams are indicative of part of the later accretion events from dwarf/ultra-faint galaxies and globular clusters (e.g. Ibata et al. 2021; Li et al. 2022; Martin et al. 2022a,b). Additionally, as much as half of the stars in the halo appears to be born *in situ*, likely consisting of both an α -rich splashed disc component (e.g. Bonaca et al. 2017; Haywood et al. 2018; Di Matteo et al. 2019; Gallart et al. 2019; Belokurov et al.

* E-mail: anke.arentsen@ast.cam.ac.uk

2020) and stars that formed in a hot and disordered pre-disc state (e.g. Belokurov & Kravtsov 2022; Conroy et al. 2022).

The common picture from various cosmological simulations suggests that the very metal-poor (VMP) stars that inhabit the spatial inner region of the Milky Way, i.e. the bulge and the disc, are amongst the oldest stars (e.g. Starkenburg et al. 2017a; El-Badry et al. 2018; Sestito et al. 2021). These stars are therefore great tracers of the early Galactic assembly. On the observational point of view, many VMP stars have been observed with such kinematics, focusing on the bulge (e.g. Howes et al. 2014, 2015, 2016; Arentsen et al. 2020; Lucey et al. 2022; Sestito et al. 2023) and the disc (e.g. Sestito et al. 2019, 2020; Di Matteo et al. 2020; Carter et al. 2021; Cordoni et al. 2021). The chemical properties of these populations indicate that the building blocks of the inner Galaxy consisted of a variety of objects – some stars appear to have formed in systems very similar to ultra-faint dwarf galaxies, while others are consistent with being born in globular cluster-like systems (e.g. Schiavon et al. 2017; Sestito et al. 2023, and references therein), and finally there may also be a significant contribution of *in situ* VMP stars in the inner Galaxy (Belokurov & Kravtsov 2022; Rix et al. 2022).

Many low-metallicity stars have been found to be carbon-enhanced metal-poor (CEMP) stars, with frequencies of the order of 30–50 per cent among stars with $[\text{Fe}/\text{H}] < -3.0$ (Beers & Christlieb 2005; Yong et al. 2013; Placco et al. 2014). There are two main types of CEMP stars. CEMP-s stars are thought to have become carbon rich later in their life due to mass transfer from a (former) asymptotic giant branch (AGB) star companion – these are typically in binary systems (e.g. Hansen et al. 2016b), are enhanced in s-process elements and carbon (a signature of AGB star nucleosynthesis), and are more frequent for $[\text{Fe}/\text{H}] > -3.0$. The CEMP-no stars are hypothesized to have been born from carbon-enhanced gas in the early Universe – they do not have s-process overabundances, are less frequently found to be in binary systems (e.g. Hansen et al. 2016a, although still more than expected, see Arentsen et al. 2019), and mostly occur at $[\text{Fe}/\text{H}] < -3.0$. The exact frequencies of CEMP-no and CEMP-s stars as a function of metallicity are still under debate (Arentsen et al. 2022), and may also vary with the Galactic environment (e.g. inner versus outer halo, bulge, dwarf galaxies, and globular clusters).

To build large samples of extremely metal-poor (EMP) stars, many dedicated searches have happened in the past 40 yr. Several different techniques have been used to identify metal-poor stars, such as following up high proper motion stars with ultraviolet excesses (Ryan & Norris 1991), identifying objects with small Ca II H&K lines in large objective-prism surveys (Beers, Preston & Shectman 1985; Christlieb et al. 2008), or using metallicity-sensitive (narrow-band) photometry (Schlaufman & Casey 2014; Starkenburg et al. 2017b; Da Costa et al. 2019; Galarza et al. 2022; Placco et al. 2022). VMP and EMP stars have also been identified in greater numbers in large-scale spectroscopic surveys such as the Sloan Digital Sky Survey (SDSS; York et al. 2000), the Large Sky Area Multi-Object Fibre Spectroscopic Telescope (LAMOST;¹ Deng et al. 2012), RAdial Velocity Experiment (RAVE; Steinmetz et al. 2006), and the GALactic Archaeology with HERMES (GALAH) spectroscopic survey (Buder et al. 2021); see e.g. Lee et al. (2013), Li, Tan & Zhao (2018), Matijević et al. (2017), and Hughes et al. (2022). These are often paired with dedicated follow-up efforts (Caffau et al. 2013; Allende Prieto et al. 2015; Bonifacio et al. 2015; Aguado et al. 2016; Placco et al. 2018; Da Costa et al. 2022; Li et al. 2022).

In this work, we combine the strengths of metallicity-sensitive photometry and large spectroscopic surveys by cross-matching metal-

poor candidates from the photometric *Pristine* survey (Starkenburg et al. 2017b) with the large data base of spectra from LAMOST, with the goal of identifying new extremely or even ultra-metal-poor stars. The *Pristine* survey uses metallicity-sensitive narrow-band CaHK photometry to derive photometric metallicities of millions of stars towards the Galactic halo, which is very efficient even for EMP stars (Youakim et al. 2017; Aguado et al. 2019). However, the selection still suffers from some more metal-rich contamination. In this work, we alleviate this by adding an extra step, namely by cross-matching candidates with $[\text{Fe}/\text{H}]_{\text{Pristine}} < -2.5$ with the LAMOST spectroscopic data base, and doing a dedicated analysis of all these (often low signal-to-noise ratio – S/N) spectra. We select exciting candidates from this analysis, and follow them up using the Optical System for Imaging and low Resolution Integrated Spectroscopy (OSIRIS) spectrograph at the 10.4-m Gran Telescopio Canarias (GTC; Cepa et al. 2000) to obtain higher S/N observations, from which we can derive high-quality metallicities to confirm their EMP nature.

We describe our initial candidate selection from *Pristine* and LAMOST in Section 2, including some discussion about the success rates. The OSIRIS observations for 11 stars and the derivation of their radial velocities (RVs), stellar parameters, distances, and orbits are described in Section 3. We present results for the OSIRIS sample in Section 4, discussing the presence of CEMP stars, the orbital properties for the sample, and a comparison with a new value-added LAMOST catalogue. We conclude in Section 5.

2 SELECTION OF EMP CANDIDATES USING *PRISTINE* AND LAMOST

The LAMOST archive contains low-resolution spectra ($R \sim 1800$) for millions of stars, but not all spectra have stellar parameters in the standard LAMOST catalogue tables. We discovered that many of the most metal-poor stars ($[\text{Fe}/\text{H}] < -2.5$) are missed by their standard pipeline (Wu et al. 2014), and also by the dedicated VMP pipeline of Li et al. (2018). This is particularly severe for hotter stars and stars with lower S/N. Other dedicated analyses might be able to deal better with these spectra, and identify promising EMP stars.

At the time our selection was made (2021 February), the latest LAMOST release was Data Release 6 (DR6). To avoid having to analyse the full data release, which contains almost 10 million spectra, we made a pre-selection of promising EMP candidates using photometric metallicities from the *Pristine* survey. We used the internal *Pristine* data release containing all CaHK observations until Semester 2020A, and adopted the CaHK+SDSS photometric metallicities (Starkenburg et al. 2017b). We queried the LAMOST archive for all stars in the *Pristine* survey with photometric metallicities $[\text{Fe}/\text{H}]_{\text{Pristine}} < -2.5$ (from using either $g - i$ or $g - r$) and $g_{\text{SDSS}} < 18$, and found ~ 7500 cross-matches for ~ 6000 unique targets. No other quality cuts were applied, which usually are included when we do dedicated target selection for *Pristine* follow-up immediately from the photometry (Youakim et al. 2017), to be as inclusive as possible.

2.1 Preliminary ULYSS analysis

A first-pass analysis of these candidates was done with the ULYSS² code (Koleva et al. 2009). ULYSS is a full-spectrum fitting package that employs empirical spectral libraries to determine stellar parameters (T_{eff} , $\log g$, $[\text{Fe}/\text{H}]$, RVs, and spectral broadening), and can be

¹<http://www.lamost.org/public/?locale=en>

²ULYSS is available from <http://ulyss.univ-lyon1.fr/>

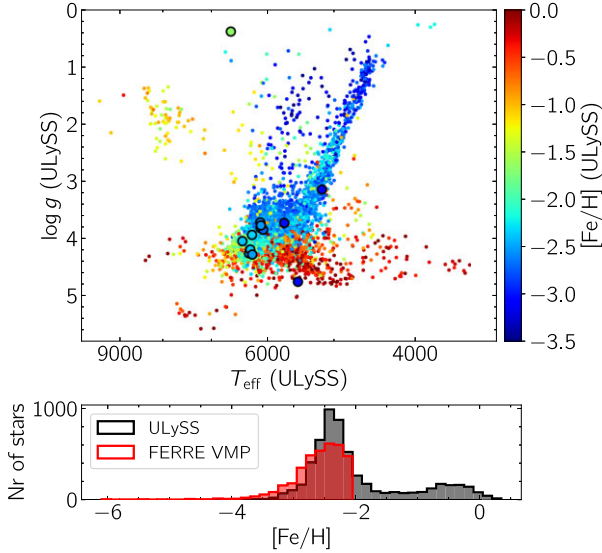


Figure 1. Top: Kiel diagram for all exposures of the 4900 unique *Pristine*-selected stars in LAMOST analysed with ULYSS, colour coded by metallicity. No quality cuts were applied to the photometric metallicities in the selection. The results for the 11 stars that were followed up with OSIRIS (see Section 3) are highlighted with larger symbols (the two high and low $\log g$ outliers are CEMP stars). Bottom: ULYSS metallicity histogram of the same sample in black, and FERRE metallicity histogram for the VMP subsample in red.

applied to stars of a wide range of stellar parameters and metallicities. We employed this code because we were interested in the types of contamination in the *Pristine* selection, which one cannot study with the dedicated metal-poor analysis described in the next subsection.

For the models, we adopted the empirical Medium-resolution INT Library of Empirical Spectra (MILES; Sánchez-Blázquez et al. 2006; Falcón-Barroso et al. 2011) and used the ULYSS MILES polynomial interpolator originally built by Prugniel, Vauglin & Koleva (2011) and updated for cool stars by Sharma, Prugniel & Singh (2016). The library has a resolving power of $R \sim 2200$, and the interpolator extends down to $[\text{Fe}/\text{H}] = -2.8$ (with the possibility to extrapolate, at one's own risk). The LAMOST spectra were fitted between 3750 and 5500 Å using a multiplicative Legendre polynomial of degree 15 for the normalization. This degree is large enough to absorb some of the large mismatches between models and observations for CEMP stars in regions of carbon-related molecular bands, which is necessary since the ULYSS models do not include $[\text{C}/\text{Fe}]$ as a free parameter, and large carbon features could mess up the normalization. There is also an automatic masking routine in ULYSS, which excludes outlier pixels iteratively and typically masks the wavelength regions of the largest carbon features in CEMP stars.

The resulting Kiel diagram and metallicity histogram from our ULYSS analysis are shown in Fig. 1, for all exposures of the ~ 4900 unique stars that remain after removing fits with signal-to-residual ratios < 8 , broadening $> 400 \text{ km s}^{-1}$ (which usually indicates a very bad fit), and duplicate LAMOST spectra for the same star. The metal-poor stars show a clear red giant branch (RGB) and main-sequence turn-off sequence, except for a small cloud of stars to the left of the RGB, which mostly consists of stars in the low S/N tail of the sample without good fits.

Most of the stars in our selection are indeed very metal poor (keeping only the fit with the highest signal-to-residual ratio per star): 71 per cent have $[\text{Fe}/\text{H}]_{\text{ULySS}} < -2.0$ and 25 per cent have $[\text{Fe}/\text{H}]_{\text{ULySS}} < -2.5$. The latter goes up to 34 per cent when using

the FERRE metallicities described later in this section, which perform better in this regime than the ULYSS metallicities, because the MILES library does not have many stars in this $[\text{Fe}/\text{H}]$ range (especially for the turn-off region). There is a contamination of metal-rich stars with $[\text{Fe}/\text{H}]_{\text{ULySS}} > -1.0$ of 16 per cent.

ULYSS is also the main software used by the LAMOST team for the parameters in their public data releases (Wu et al. 2014). They use the interpolator based on the ELODIE library (Prugniel & Soubiran 2001; Wu et al. 2011), which has a more limited coverage of the parameter space compared to MILES, and extends only down to $[\text{Fe}/\text{H}] = -2.5$. Of the stars that have $[\text{Fe}/\text{H}]_{\text{ULySS}} < -2.0 / -2.5$ in our analysis, only 30 per cent/17 per cent have stellar parameters in the public LAMOST Data Release 7 (DR7) catalogue. This is likely partly due to the ELODIE library being less good at low metallicities, and partly due to more stringent quality cuts being applied for stars to make it into the LAMOST data releases.

2.2 Success rates

In our original selection, we did not make any additional photometric quality cuts. The *Pristine* team developed several quality cuts to remove metal-rich outliers and improve the success rates of the spectroscopic follow-up of EMP candidates. The cuts applied for the main *Pristine* follow-up campaign are discussed in section 4.1 of Youakim et al. (2017). We apply very similar cuts to the *Pristine*+LAMOST sample to see how that changes the metallicity distribution, keeping only the stars that have

- (i) CASU flag = -1 or 1 ;
- (ii) young stars flag = 0 ;
- (iii) $(u_0 - g_0) > 0.6$;
- (iv) $0.25 < (g_0 - i_0) < 1.5$ and $0.15 < (g_0 - r_0) < 1.2$;
- (v) $[\text{Fe}/\text{H}]_{\text{Pristine}} < -2.5$ (from using either SDSS $g - i$ or $g - r$) and $\neq -99$ (-99 is assigned if the star falls outside of the parameter space for which the photometric metallicity assignment has a valid calibration);
- (vi) instead of the Panoramic Survey Telescope and Rapid Response System (Pan-STARRS) variability catalogue as in Youakim et al. (2017), we use the *Gaia* photometric variability to remove variable stars as in Fernández-Alvar et al. (2021).

The uncertainties on $[\text{Fe}/\text{H}]_{\text{Pristine}}$ are not taken into account here, whereas they were in Youakim et al. (2017). After applying the above cuts, the sample goes from 4900 stars to 4100 stars again keeping the highest signal-to-residual spectrum per star. Of these, 78 per cent have $[\text{Fe}/\text{H}]_{\text{ULySS}} < -2.0$, and 28 per cent have $[\text{Fe}/\text{H}]_{\text{ULySS}} < -2.5$ (the latter goes up to 38 per cent for the FERRE metallicities), compared to the previous 71 per cent and 25 per cent (and 34 per cent for FERRE), respectively. The metal-rich contamination goes down to 12 per cent. Doing the same only for stars with signal-to-residual ratios > 20 instead of our initial cut at > 8 , the results are very similar. We conclude that, for the *Pristine*+LAMOST sample, the photometric quality cuts slightly improve the selection efficiency, but not by a lot.

The success rate of previous *Pristine* follow-up for $[\text{Fe}/\text{H}]_{\text{Pristine}} < -2.5$ was found to be 56 per cent (Aguado et al. 2019). The lower fraction in this work (38 per cent when applying the photometric quality cuts and adopting the FERRE metallicities) could be due to various reasons. For example, the dedicated *Pristine* follow-up presented in Youakim et al. (2017) and Aguado et al. (2019) focused on the most metal-poor stars, and did not homogeneously observe *all* stars with $[\text{Fe}/\text{H}]_{\text{Pristine}} < -2.5$. Additionally, extra quality cuts were sometimes implemented for subsets of the follow-

Table 1. List of 481 EMP candidates (533 spectra) with FERRE spectroscopic parameters used for target selection. No quality cuts have been applied. The first few lines of the table are shown here for guidance, the full table and figures showing the best fits are available as online supplementary material.

LAMOST spectrum name	Gaia DR3 source.id	RA ($^{\circ}$)	Dec. ($^{\circ}$)	T_{eff} (K)	$\log g$ (cgs)	[Fe/H]	[C/Fe]	S/N	$\log(\chi^2)$
spec-56746-HD121251N314746M01_sp02-087	4014278062082321152	181.215811	30.331285	6232 ± 325	5.0 ± 1.4	-3.7 ± 15.1	-0.4 ± 90.4	6	-0.338
spec-57308-EG000023N024031M01_sp03-076	2739551594198812160	358.800705	2.493245	6521 ± 161	4.7 ± 0.4	-3.2 ± 0.8	0.1 ± 6.9	24	-0.214
spec-57754-HD122624N271605M02_sp03-108	4009964020835772288	185.239126	27.687022	5675 ± 57	4.3 ± 0.3	-3.4 ± 0.1	0.3 ± 0.3	34	-0.123
...

up presented in Aguado et al. (2019), most notably the consistency of the photometric temperatures derived from SDSS between ($g - i$) and ($g - r$). If we select only stars with $[\text{Fe}/\text{H}]_{\text{Pristine}} < -2.7$ and $|T_{\text{eff}}(g-i) - T_{\text{eff}}(g-r)| < 200$ K, the success rate in this work for $[\text{Fe}/\text{H}]_{\text{FERRE}} < -2.5$ goes up to 50 per cent, and the contamination of stars with $[\text{Fe}/\text{H}]_{\text{ULYSS}} > -1.0$ is reduced from 12 per cent to 2 per cent.

The numbers in this section are not meant to override the previously published *Pristine* success rates by Youakim et al. (2017) and Aguado et al. (2019). Our results confirm that the success rates are high, and highlight some of the subtleties in deriving such success rates. Overall we conclude that our methodology to find hidden VMP and EMP stars in the large LAMOST data base is extremely efficient.

2.3 Dedicated VMP FERRE analysis

A dedicated very metal-poor (VMP) analysis was performed for the subsample of LAMOST spectra with $[\text{Fe}/\text{H}]_{\text{ULYSS}} < -2.0$, with the aim of deriving better metallicities and carbon abundances for the most metal-poor stars and identifying potential ultra-metal-poor candidates. We followed a similar methodology as in Aguado et al. (2017a,b), using the FERRE³ code (Allende Prieto et al. 2006). The code interpolates between the nodes of a library of synthetic spectra and derives simultaneously the set of best stellar parameters (T_{eff} , $\log g$, $[\text{Fe}/\text{H}]$, and $[\text{C}/\text{Fe}]$). For this preliminary analysis, we used the default Nelder–Mead search algorithm and linear interpolation. The dedicated VMP synthetic models were computed with the ASSET code (Koesterke, Allende Prieto & Lambert 2008) and published in Aguado et al. (2017b) with the following parameter coverage:

- (i) $4750 < T_{\text{eff}} < 7000$ K, $\Delta T_{\text{eff}} = 250$ K;
- (ii) $1.0 < \log g < 5.0$, $\Delta \log g = 0.5$;
- (iii) $-6.0 < [\text{Fe}/\text{H}] < -2.0$, $\Delta[\text{Fe}/\text{H}] = 0.5$;
- (iv) $-1.0 < [\text{C}/\text{Fe}] < +5.0$, $\Delta[\text{C}/\text{Fe}] = 1.0$;

and a fixed $[\alpha/\text{Fe}] = +0.4$ and $[\text{N}/\text{Fe}] = 0$. Both the data and the models were continuum normalized with a running mean filter with a 30-pixel window. We limited the fit to the wavelength range 3700–5500 Å, where most of the features for EMP stars are present. The spectra were shifted to rest wavelength using the ULYSS RVs.

The resulting metallicity distribution is shown in red in the bottom panel of Fig. 1, without any additional quality cuts applied. The hard limit at $[\text{Fe}/\text{H}]_{\text{FERRE}} = -2.0$ is due to the limit of the grid. The ULYSS and FERRE distributions peak at roughly the same metallicities, but the FERRE distribution has a larger tail towards lower metallicities – as expected.

We inspected the >500 fits in the resulting FERRE-analysed sample with $[\text{Fe}/\text{H}]_{\text{FERRE}} < -3.0$ by eye, and identified a number of (previously unknown) stars of interest that could potentially have $[\text{Fe}/\text{H}] < -4.0$ or that looked very carbon rich and extremely

metal poor ($[\text{Fe}/\text{H}] < -3.0$). Practically none of our candidates had parameters in the public DR6 catalogue. Most of our candidates had relatively low S/N, so follow-up spectroscopy was necessary to confirm their extremely or even ultra-metal-poor nature.

The full list of EMP candidates that we inspected is given in Table 1, with figures for all the spectral fits provided in the online supplementary materials. This candidate list with its derived parameters should not be used blindly since no quality cuts have been applied (on e.g. S/N, $\log(\chi^2)$, or parameter uncertainties), but it could be used in combination with the figures to select other EMP stars for follow-up. Stars may occur multiple times in this list if they have more than one LAMOST spectrum.

3 OSIRIS FOLLOW-UP OF EMP CANDIDATES

We obtained GTC/OSIRIS observations for 11 of our most promising candidates ($16.9 < g < 17.9$) in Semester 2021A. We used OSIRIS in long-slit mode with the 2500U grating, a 1-arcsec slit and 2×2 binning, resulting in spectra covering 3440–4610 Å at a resolving power $R \sim 2400$ [providing an instrument profile with a full width at half-maximum (FWHM) of ~ 125 km s⁻¹]. We aimed for an S/N of 40 at 4000 Å, corresponding to exposure times of 3000 s for stars of magnitude $g \sim 17.5$. A summary of the observations is presented in Table 2. Individual exposures of 1400, 1600, and 1800 s were executed for different targets.

3.1 Radial velocities

Radial velocities (RVs) are derived using the cross-correlation technique. We have a high-quality GTC/OSIRIS spectrum of a bright EMP star G64-12 ($T_{\text{eff}} = 6463$ K, $\log g = 4.26$, $[\text{Fe}/\text{H}] = -3.29$, $[\text{C}/\text{Fe}] = +1.07$; Placco et al. 2016 and references therein) from previous campaigns acquired with the same set-up (Aguado et al. 2017a, 2018) that we use as a cross-correlation template. The OSIRIS spectra of both our targets and the template star are normalized with the same method, using a running mean filter with a width of 30 pixels. We built the cross-correlation function (CCF) with our own IDL-based automated code in the spectral range 3755–4455 Å with a window of 3000 km s⁻¹. The main features in the template are the Ca II H&K lines, the H I lines of the Balmer series, and the G-band in carbon-enhanced stars (see Fig. 2). The normalization method produces a shape of the CCF profile that mimics the shape of all Balmer lines in the warm template EMP star, which does not resemble a Gaussian shape. We thus fit the CCF profile with a parabolic fit using the closest six points to the CCF peak. The statistical uncertainty of the centroid of the parabolic fit is typically below 1 km s⁻¹, significantly below the pixel size of ~ 0.57 Å pixel⁻¹ (~ 42 km s⁻¹ pixel⁻¹). The results of the OSIRIS spectra show intranight RV variations with standard deviations below ~ 7 km s⁻¹, but RV variations from different nights with standard deviations in the range 3–20 km s⁻¹.

³FERRE is available from <http://github.com/callendeprieto/ferre>

Table 2. Summary of the OSIRIS observations: our reference for each star, the LAMOST and *Gaia* DR3 designations, positions, SDSS magnitudes in *u* and *g*, total exposure time, signal-to-noise ratio (S/N) at two different wavelengths, number of observations, and date that the spectra were observed.

Star #	LAMOST designation	<i>Gaia</i> DR3 source_id	RA	Dec.	<i>u</i> (mag)	<i>g</i> (mag)	Total exp time (s)	S/N (@392/450 nm)	Nobs	Date observed (DD-MM-2021)
LP1	J002953.07+320229.9	2862648994739368704	00:29:53.07	32:02:29.9	18.49	17.58	2800	33/79	2	14-07
LP2	J131532.41+121107.4	3736550805114696192	13:15:32.41	12:11:07.4	18.33	17.44	2800	57/127	2	11-04
LP3	J134510.95+424910.8	1500794652785646976	13:45:10.96	42:49:10.9	17.75	16.94	1400	74/180	1	15-06
LP4	J142055.86+075308.7	3673778479398720000	14:20:55.87	07:53:08.7	17.96	17.04	1400	62/100	1	15-06
LP5	J144714.22+163425.4	1186662458446883328	14:47:14.22	16:34:25.5	18.73	17.92	2800	27/88	2	10-06
LP6	J145214.98+160357.6	1186397549159479424	14:52:14.99	16:03:57.7	18.25	16.88	1400	12/97	1	10-06
LP7	J145611.30+161925.7	1187873604865113472	14:56:11.31	16:19:25.8	18.77	17.82	4600	34/116	3	08-04
LP8	J161021.42+451247.5	1386190837835580288	16:10:21.43	45:12:47.6	18.50	17.63	5600	30/79	4	10-06/17-07
LP9	J162359.32+303740.8	1318369490300720000	16:23:59.32	30:37:40.9	18.46	17.52	5600	24/78	4	11-04/14-07
LP10	J212109.07+151328.7	1783524305407324672	21:21:09.06	15:13:29.0	18.15	17.15	4800	38/145	3	15-06/13-07/14-07
LP11	J230209.39+302100.6	1886140596052059392	23:02:09.39	30:21:00.7	18.01	17.09	3600	39/192	2	23-05/13-07

We also derive the RV for the same stars from their LAMOST spectra (which typically have much lower S/N than the OSIRIS spectra), using the same technique to check the consistency with our OSIRIS RVs. The LAMOST spectrum of G64-12 is used as cross-correlation template and all spectra are normalized using a running mean filter with a width of 15 pixels of $\sim 1.38 \text{ \AA pixel}^{-1}$ ($\sim 81 \text{ km s}^{-1} \text{ pixel}^{-1}$). The CCF is built from the spectral range 3755–6755 \AA , which includes H α and H β , providing more stability to the CCF profile given the lower quality LAMOST spectra. We find a reasonable consistency when comparing to the OSIRIS results, with a mean difference of -4.4 km s^{-1} and a standard deviation of 15.9 km s^{-1} .

For each target we adopt the weighted mean of the OSIRIS RVs derived from each individual spectrum and the corresponding error of the mean as the final RV. We apply a quadratically added uncertainty floor of 15 km s^{-1} to the RV uncertainties, which seems more realistic than the CCF uncertainties given the RV variations within and between different nights and the differences with the LAMOST RVs. This floor reflects the systematic RV uncertainty due to possible instrument flexures, pointing, guiding RV drifts, etc.

3.2 Distances

It has been widely demonstrated that simply inverting the parallax to infer the distance can lead to wrong results, and including additional priors and/or data improves distance estimates (e.g. Bailer-Jones et al. 2018, 2021; Anders et al. 2022). This is especially the case when the parallax has poor measurements, i.e. $\varpi < 0$ and/or $\varpi/\sigma_\varpi < 20$. We therefore use a Bayesian approach to infer the distances for the stars in our sample. The probability distribution function (PDF), or posterior, is inferred following the method fully described in Sestito et al. (2019). Briefly, the likelihood is the product of the Gaussian distributions for the parallax and photometry. The prior takes into account a power-law stellar distribution (see the halo prior in Sestito et al. 2019), and, through a set of VMP ([M/H] = -2.5) MESA/MIST isochrones⁴ (Choi et al. 2016; Dotter 2016), the knowledge that VMP stars are old (11–13.8 Gyr), low mass ($< 1 M_\odot$), and distributed with a given initial mass function (IMF)-based luminosity function in the colour–magnitude diagram (CMD). The zero-point offset has been applied to the *Gaia* Data Release 3 (DR3) parallaxes (Lindgren et al. 2021) using the PYTHON GAIADR3_ZEROPOINT⁵ package. This

method, widely used for chemo-dynamical investigations of VMP stars (e.g. Sestito et al. 2019, 2020; Venn et al. 2020), produces low uncertainties on the distances even in case of large parallax uncertainties. This is because the isochrones limit the possible distances for a star with a given colour to two different solutions, a dwarf and a giant solution, and nothing in between. The parallax would then typically prefer one of the two, or, in case of a very poor parallax measurement, the two peaks would be given a different probability. We calculate the probabilities following Sestito et al. (2019). For seven of the OSIRIS stars the probability of the main peak is larger than 92 per cent. For two stars it is 86 per cent (LP1, although for this star we adopt the less probable solution, see Section 4.1) and 87 per cent (LP5), while for the remaining two stars it is 54 per cent (LP8) and 66 per cent (LP2).

3.3 Orbital parameters

The orbital parameters are inferred using GALPY⁶ (Bovy 2015). The code requires as input the inferred distances, the RVs, and the proper motions and coordinates from *Gaia* DR3. The total fixed gravitational potential that we adopt is the sum of a Navarro–Frenk–White dark matter halo (Navarro, Frenk & White 1997, NFWPOTENTIAL), a Miyamoto–Nagai potential disc (Miyamoto & Nagai 1975, MIYAMOTONAGAI-POTENTIAL), and an exponentially cut-off bulge (POWERSPHERICALPOTENTIALWCUTOFF). All of the aforementioned potentials are usually invoked by the MWPOTENTIAL14 package. However, we adopt a more massive and up-to-date halo (Bland-Hawthorn & Gerhard 2016), with a mass of $1.2 \times 10^{12} M_\odot$ (versus $0.8 \times 10^{12} M_\odot$ for MWPOTENTIAL14).

For each star, we perform a Monte Carlo simulation with 1000 random draws on the input parameters to infer the orbital parameters and their uncertainties. In case of the proper motion components, we consider their correlation given the coefficients from *Gaia* DR3, drawing randomly with a multivariate Gaussian function. The RVs (from the OSIRIS spectra) and coordinates are treated as a Gaussian. In order to account for possible systematics on the distances (e.g. due to the adopted isochrones and other assumptions), we assume a 15 per cent uncertainty on the distances. The integration time is set to 1 Gyr. The orbital parameters are inferred for both of the peaks in the distance PDFs.

The output orbital parameters are the Galactocentric Cartesian coordinates (*X*, *Y*, *Z*), the maximum distance from the Milky Way plane Z_{max} , the apocentric and pericentric distances (R_{apo} , R_{peri}), the

⁴<https://waps.cfa.harvard.edu/MIST/>

⁵https://gitlab.com/icc-ub/public/gaiadr3_zero_point

⁶<http://github.com/jobovy/galpy>

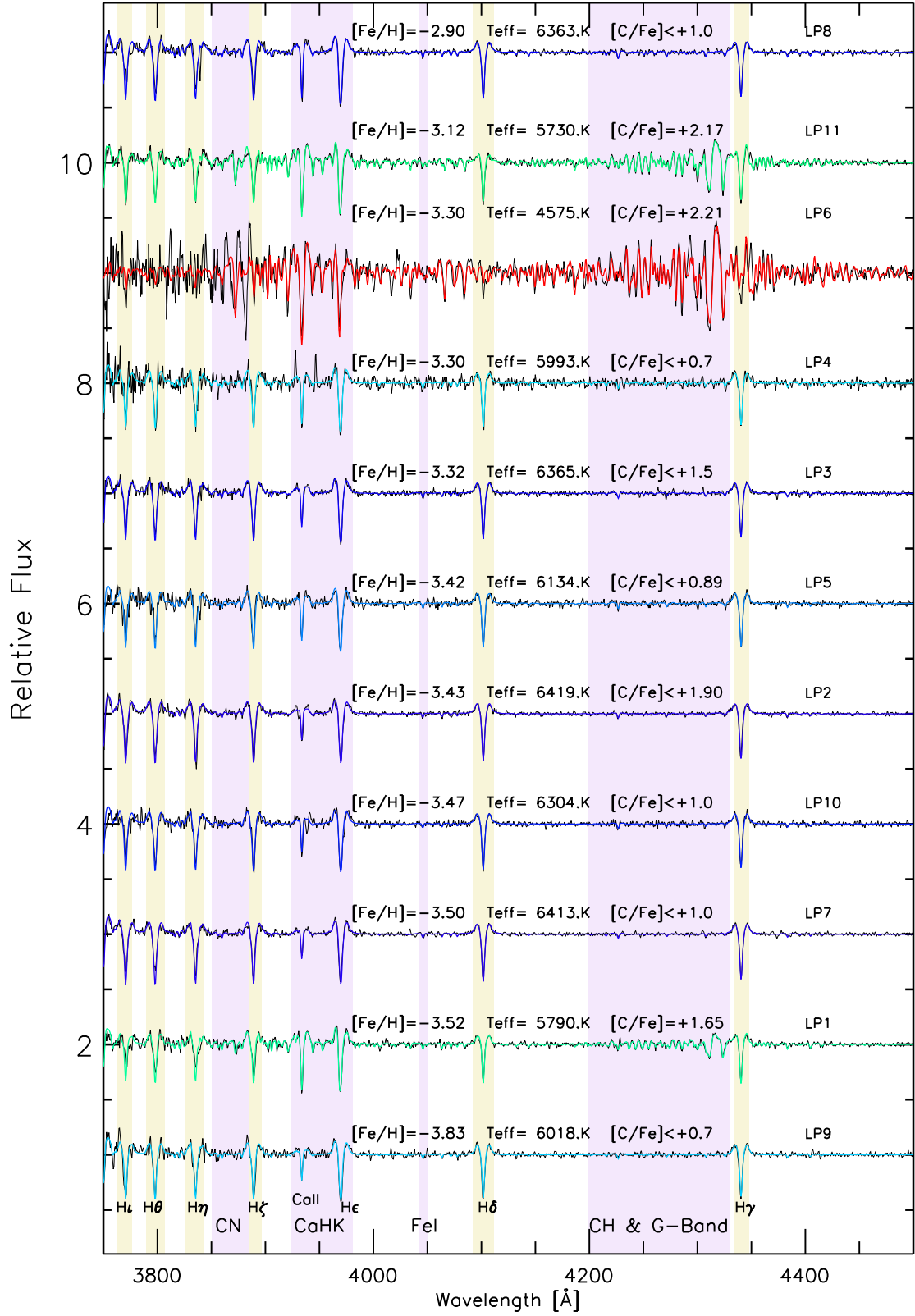
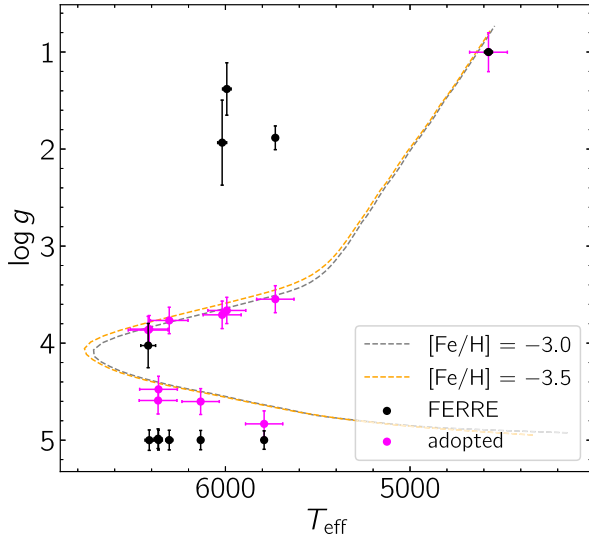


Figure 2. OSIRIS/GTC spectra (3750–4500 Å) of our stellar sample (black line) and the best fits calculated with FERRE, colour coded by T_{eff} (the bluer the hotter) and sorted by decreasing $[\text{Fe}/\text{H}]$. The Balmer lines (yellow) and main metallic absorption features (purple) are highlighted. Above each spectrum the metallicity, effective temperature, and carbonicity are displayed.

Table 3. Radial velocities (RVs), heliocentric distance, probability of the distance within 3σ around the maximum of the distance PDF, maximum height from the plane, apocentric and pericentric distances, eccentricity, energy, the action vector are reported.

Star #	RV (km s ⁻¹)	D (kpc)	P _D	Z _{max} (kpc)	R _{apo} (kpc)	R _{peri} (kpc)	ε	E/10 ⁴ (kpc km ² s ⁻²)	J _φ (kpc km s ⁻¹)	J _r (kpc km s ⁻¹)	J _z (kpc km s ⁻¹)
LP1	-18 ± 15	8.62 ± 0.47	0.14	15.6 ^{+4.9} _{-4.4}	16.2 ^{+6.8} _{-3.1}	2.4 ^{+1.3} _{-0.8}	0.75 ^{+0.04} _{-0.03}	-4.79 ^{+1.29} _{-0.86}	-140 ⁺³⁶⁵ ₋₄₁₇	829 ⁺¹⁷⁷ ₋₁₄₂	780 ⁺²¹⁵ ₋₃₂₉
LP2	211 ± 15	6.88 ± 0.15	0.66	15.5 ^{+12.6} _{-4.7}	24.3 ^{+31.4} _{-9.4}	8.5 ^{+0.8} _{-0.7}	0.52 ^{+0.19} _{-0.19}	-2.76 ^{+2.17} _{-1.63}	-1821 ⁺⁴⁰⁵ ₋₄₃₄	17 ⁺¹ ₋₁	905 ⁺³⁰⁶ ₋₁₅₃
LP3	-162 ± 15	2.35 ± 0.12	0.99	8.0 ^{+1.6} _{-1.5}	9.8 ^{+0.5} _{-0.4}	2.4 ^{+0.7} _{-0.7}	0.60 ^{+0.10} _{-0.10}	-6.62 ^{+0.15} _{-0.13}	368 ⁺¹⁹⁷ ₋₂₂₃	294 ⁺⁸⁷ ₋₇₆	501 ⁺¹⁸⁸ ₋₁₄₅
LP4	-70 ± 15	6.03 ± 0.10	1.0	7.5 ^{+0.3} _{-1.3}	7.8 ^{+0.2} _{-0.5}	1.5 ^{+0.9} _{-0.6}	0.66 ^{+0.12} _{-0.13}	-7.58 ^{+0.36} _{-0.22}	-15 ⁺²⁰⁷ ₋₁₉₅	200 ⁺⁶³ ₋₆₀	556 ⁺¹⁵⁹ ₋₁₇₅
LP5	-126 ± 15	3.25 ± 0.16	0.87	5.3 ^{+1.4} _{-0.8}	10.1 ^{+0.4} _{-0.3}	2.9 ^{+0.5} _{-0.5}	0.54 ^{+0.06} _{-0.06}	-6.50 ^{+0.14} _{-0.14}	750 ⁺¹⁵¹ ₋₁₅₁	269 ⁺⁵⁶ ₋₄₉	259 ⁺⁷⁶ ₋₆₄
LP6	53 ± 15	22.7 ± 1.4	1.0	21.2 ^{+3.3} _{-3.6}	21.7 ^{+5.7} _{-3.6}	11.8 ^{+6.3} _{-3.5}	0.30 ^{+0.06} _{-0.08}	-3.02 ^{+1.16} _{-0.81}	576 ⁺⁴⁰⁷ ₋₂₀₃	198 ⁺⁴³ ₋₆₁	2480 ⁺⁷⁷⁰ ₋₅₂₇
LP7	-136 ± 15	8.05 ± 0.18	0.92	36.2 ^{+48.7} _{-22.3}	52.8 ^{+135.8} _{-35.2}	7.7 ^{+1.1} _{-0.7}	0.74 ^{+0.16} _{-0.27}	-0.85 ^{+4.15} _{-3.23}	-1583 ⁺¹⁸⁹ ₋₉₉	38 ⁺¹ ₋₁	1382 ⁺⁸⁸⁹ ₋₅₇₅
LP8	-56 ± 15	3.62 ± 0.23	0.54	2.8 ^{+0.6} _{-0.5}	9.2 ^{+0.4} _{-0.3}	4.6 ^{+0.5} _{-0.5}	0.33 ^{+0.05} _{-0.05}	-6.48 ^{+0.18} _{-0.15}	1215 ⁺¹⁰⁷ ₋₁₁₄	109 ⁺³⁸ ₋₂₇	112 ⁺²⁵ ₋₂₃
LP9	-254 ± 15	7.25 ± 0.14	0.99	31.8 ^{+50.0} _{-19.8}	39.9 ^{+90.7} _{-20.9}	3.6 ^{+1.8} _{-0.7}	0.83 ^{+0.08} _{-0.09}	-1.61 ^{+3.56} _{-2.59}	-726 ⁺¹⁹⁶ ₋₁₁₅	269 ⁺¹⁰ ₋₁₀	903 ⁺⁹⁴³ ₋₅₂₈
LP10	-361 ± 15	5.79 ± 0.10	0.93	23.3 ^{+10.4} _{-11.3}	52.4 ^{+115.2} _{-28.8}	5.1 ^{+0.8} _{-0.4}	0.83 ^{+0.10} _{-0.13}	-0.70 ^{+3.49} _{-2.44}	-1185 ⁺²³⁴ ₋₁₈₂	191 ⁺¹⁰ ₋₁₀	957 ⁺⁷⁶⁹ ₋₅₀₀
LP11	-68 ± 15	6.09 ± 0.10	0.99	12.5 ^{+6.6} _{-3.9}	15.7 ^{+8.4} _{-3.9}	10.5 ^{+0.7} _{-0.8}	0.21 ^{+0.16} _{-0.09}	-3.89 ^{+1.17} _{-0.78}	1467 ⁺¹⁴¹ ₋₁₁₆	58 ⁺²⁵⁵ ₋₅₇	1084 ⁺⁴⁶⁵ ₋₃₃₆

**Figure 3.** Kiel diagram showing the pure FERRE stellar parameters (black) and the adopted stellar parameters and uncertainties (magenta). See the text for details. Also shown are Yonsei–Yale isochrones for two different metallicities (both with age = 12 Gyr, $[\alpha/\text{Fe}] = +0.4$).

eccentricity ϵ , the energy E , and the spherical actions coordinates (J_ϕ , J_r , J_z). Table 3 reports the main orbital parameters from the most probable distance, except for star LP1 where we adopt the less probable distance (see Section 4.1). The orbital parameters are discussed in Section 4.1.

3.4 Stellar parameters

The OSIRIS data were analysed with FERRE in a similar manner as the LAMOST spectra. For this analysis we use the more sophisticated Boender–Timmer–Rinnoy Kan (BTRK; Boender et al. 1982) global search algorithm and Bézier cubic interpolation. We use the same grid, except for the coolest star in the sample, for which we employ a similar grid that has been extended down to 4500 K (as used e.g. in Arentsen et al. 2021). Again we used a 30-pixel window for the running mean normalization, suitable for OSIRIS resolution ($R = \lambda/\delta\lambda \sim 2400$). To avoid problems in

the noisy blue region we only analyse the spectra in the range (3750–4500 Å).

We found that for the warm stars in the sample (with $T_{\text{eff}} > 5500$ K, which is all stars except for LP6), the $\log g$ values that FERRE finds are typically at the edges of the FERRE grid, e.g. at $\log g = 5.0$ or $\log g < 2.0$, see the black points in Fig. 3. This is likely the result of not much $\log g$ information being present in these EMP stars in the available wavelength range. Previous work on metal-poor stars with FERRE has shown that systematically offset $\log g$ values strongly impact the derived $[\text{C}/\text{Fe}]$ (Aguado et al. 2019; Arentsen et al. 2021). Therefore we decided to adopt photometric $\log g$ values for the warm stars, shown by the magenta points in Fig. 3. These were inferred from the Stefan–Boltzmann equation, which needs as input the dereddened absolute G magnitude (derived using the *Gaia* G -band magnitude, the 3D extinction map from Green et al. 2019 and the distances from Table 3), an estimate of the effective temperature, and the bolometric corrections on the flux (Andrae et al. 2018). We adopt the FERRE effective temperature and its inflated uncertainty (see last paragraph of this subsection) in the calculation. We perform a Monte Carlo iteration with 1000 random draws on the input parameters. Each of them is described by a Gaussian distribution.

We run FERRE again for the warm stars, fixing the T_{eff} to the previously derived FERRE value and $\log g$ to the photometric values, while letting $[\text{Fe}/\text{H}]$ and $[\text{C}/\text{Fe}]$ free. The final spectral fits are shown in Fig. 2 and a summary of the results is provided in Table 4. The differences between the original FERRE run and the run with fixed T_{eff} and $\log g$ are small for the metallicities, with the adopted $[\text{Fe}/\text{H}]$ being higher by 0.07 dex with a standard deviation of 0.06 dex. The differences for $[\text{C}/\text{Fe}]$ are also small for the stars with original $\log g > 4$ and measured $[\text{C}/\text{Fe}]$ (see next section), they are 0.05 on average, with a standard deviation of 0.09 dex. However, for the one star with measured carbon and FERRE $\log g < 3$ (LP11), the new $[\text{C}/\text{Fe}]$ is 0.7 dex lower.

There are three stars (LP4, LP7, and LP9) that have very high FERRE internal $[\text{Fe}/\text{H}]$ uncertainties of 0.5–1.0 dex when calculated by inverting the covariance matrix (our original approach). This could be attributed to some negative/zero fluxes in blue end of the OSIRIS data. To avoid this issue we recalculated the internal FERRE uncertainties using a Monte Carlo simulation. We performed 50 experiments and use the dispersion on the derived $[\text{Fe}/\text{H}]$ and $[\text{C}/\text{Fe}]$ as the uncertainty following Aguado et al. (2017a). As a

Table 4. Adopted stellar parameters with T_{eff} , [Fe/H], and [C/Fe] from FERRE and photometric $\log g$.

Star #	T_{eff} (K)	$\log g$ (cgs)	[Fe/H]	[C/Fe] $A(\text{C})_{\odot} = 8.39^a$	Corr. ^b
LP1	5790 ± 101	4.83 ± 0.22	-3.52 ± 0.11	$+1.65 \pm 0.21$	
LP2	6419 ± 108	3.85 ± 0.30	-3.43 ± 0.12	$< +1.90$	
LP3	6365 ± 102	4.57 ± 0.08	-3.32 ± 0.11	$< +1.5$	
LP4	5993 ± 103	3.65 ± 0.28	-3.30 ± 0.11	$< +0.70$	
LP5	6134 ± 102	4.59 ± 0.37	-3.42 ± 0.11	$< +0.89$	
LP6	4575 ± 103	1.00 ± 0.20	-3.30 ± 0.11	$+2.21 \pm 0.21$	+0.24
LP7	6413 ± 103	3.85 ± 0.39	-3.50 ± 0.11	$< +1.0$	
LP8	6363 ± 103	4.47 ± 0.19	-2.90 ± 0.11	$< +0.96$	
LP9	6018 ± 103	3.70 ± 0.21	-3.83 ± 0.12	$< +0.70$	
LP10	6304 ± 102	3.75 ± 0.14	-3.47 ± 0.11	$< +1.02$	
LP11	5730 ± 102	3.53 ± 0.24	-3.12 ± 0.13	$+2.17 \pm 0.22$	

^aSolar abundance adopted from Asplund, Grevesse & Sauval (2005).^bEvolutionary [C/Fe] correction following Placco et al. (2014).

result of that the issue with the large uncertainties was fixed for the three problematic stars, and the uncertainties for the other stars remain the same within 0.01–0.02 dex. We adopt the Monte Carlo internal uncertainties.

To provide the final uncertainties for the stellar parameters, we add estimates of the external uncertainties from a previous analysis of EMP stars with FERRE (Aguado et al. 2017a) to our internal FERRE uncertainties. These are 100 K, 0.1 and 0.2 dex for T_{eff} , [Fe/H] and [C/Fe], respectively. For [Fe/H] and [C/Fe] we adopt the internal uncertainties from the first FERRE run, because the second run does not properly reflect the real uncertainties since it fits only two of the four parameters. For $\log g$, we adopted the uncertainties from the photometric determination for the warm stars, and for the coolest star we quadratically added 0.2 dex of external uncertainties (Aguado et al. 2017a) to the internal FERRE uncertainty. The results are shown in Table 4.

3.5 Carbon determination

Deriving carbon abundance from low-resolution data of EMP stars is non-trivial. Our employed grid is suitable for the analysis of CEMP stars, since carbon enhancement was not only considered in the spectral synthesis step but also in the ATLAS stellar models (Sbordone, Bonifacio & Castelli 2007). This is crucial because high carbon abundances can significantly impact the stellar atmospheres. The grid of models has been used successfully to derive carbon abundances in several works (e.g. Aguado et al. 2017a,b, 2019; Arentsen et al. 2021, 2022), although there are some differences with other synthetic grids that can lead to systematic differences in derived carbon abundances (Arentsen et al. 2022). This is likely related to the use of different codes, line lists, and assumptions (e.g. different [N/Fe] abundances).

The ability of the FERRE code to detect – and successfully fit – carbon absorption features from low-resolution data strongly depends on (a) T_{eff} (and $\log g$ to a lesser extent), (b) the carbon abundance, and (c) the S/N of the spectra. In our sample there are three stars (LP1, LP6, and LP11) that fulfil the sensitivity criteria derived by Aguado et al. (2019) based on these parameters, all of them have $T_{\text{eff}} < 6000$ K and show strong CH absorption features. For these objects we derived [C/Fe] = +1.65/ +2.21/ +2.17 respectively, with reasonable uncertainties (~ 0.2 dex). For the other stars we can only provide upper limits on the carbon abundances. The carbon results are summarized in Table 4.

The object with the lowest T_{eff} in our sample, LP6, shows clear CN features at ~ 3885 Å that our best fit is not able to reproduce, although the CH & G-band fit is good (see Fig. 2, red spectrum). The reason for this is that our FERRE synthetic spectral library assumes [N/Fe] = 0.0 for all stellar models. Querying the high-resolution spectroscopy compilation in the JINABase (Abomalima & Frebel 2018) for stars with $-3.5 < [\text{Fe}/\text{H}] < -3.0$, we find that all of those with measured nitrogen abundances have [N/Fe] > 0, and stars with [C/Fe] > +2.0 typically have $1.5 < [\text{N}/\text{Fe}] < 3.0$. This is very different from the assumed [N/Fe] in the FERRE grid, and can explain why the CN band for LP6 is much stronger in the data than in the model fit. However, the fit reproduces quite well the Ca II at 3933 Å and several other Fe I, Ti II, and Sr II lines in the 4040–4080 Å region. Additionally, the majority of the carbon information is significantly concentrated around the G-band (4200–4330 Å) and our fit is good in that area. Therefore, we conclude that the CN absorption features in the blue are not significantly affecting the best fit for this object.

The carbon abundance of evolved giants decreases with decreasing $\log g$ due to mixing processes, especially in metal-poor stars (Gratton et al. 2000; Placco et al. 2014). We estimate the evolutionary carbon correction for the most evolved star in our sample (LP6, the only star that should be affected by this effect) using the web calculator⁷ by V. M. Placco, and find it to be +0.24 dex.

4 OSIRIS SAMPLE RESULTS

The derived properties for our 11 OSIRIS stars are summarized in Tables 3 and 4. In this section, we will use these parameters to study the Galactic orbital properties of our sample, to study the CEMP stars in our sample, and to make a comparison with a recent LAMOST catalogue that includes VMP stars.

4.1 Orbital properties

Here we discuss the orbital parameters for our EMP OSIRIS sample. We adopted the results for the most probable distance solution (see Section 3.2), except for LP1 for which the most probable solution leads to an unbound orbit – we therefore prefer the less probable distance solution for this star. The five panels in Fig. 4 display the main orbital parameters typically used to classify the kinematic properties

⁷<https://vplacco.pythonanywhere.com/>

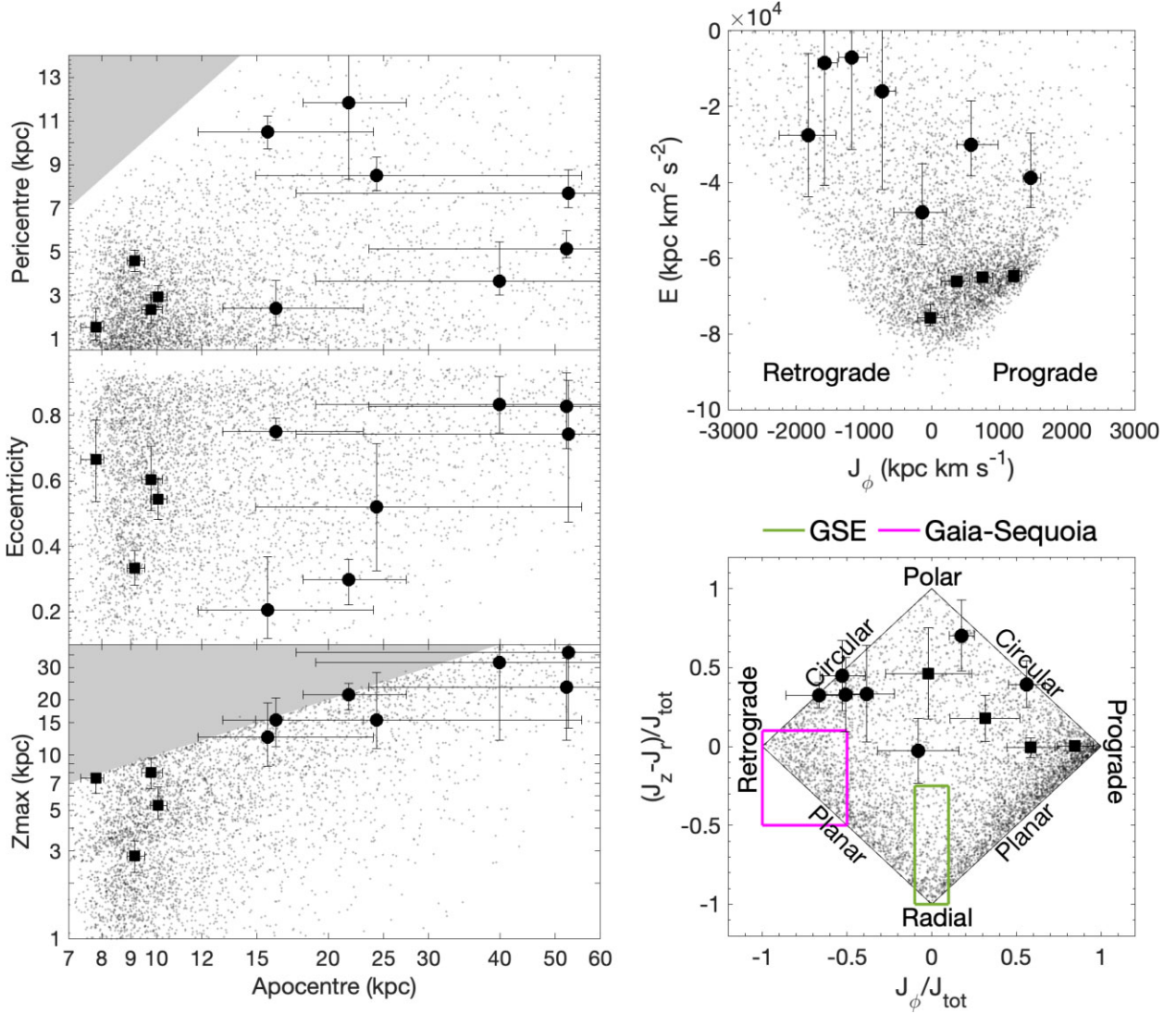


Figure 4. Orbital parameters. Three left-hand panels: pericentre, eccentricity, and maximum distance from the Milky Way plane as a function of the apocentric distance. The grey-shaded areas denote the forbidden region in which the $Z_{\max} > R_{\text{apo}}$ or $R_{\text{peri}} > R_{\text{apo}}$. Upper right-hand panel: energy versus rotational component of the action, J_{ϕ} . Bottom right-hand panel: action space; the y-axis is the difference between the vertical and radial component of the action, while the x-axis is the rotational component; axes are normalized by $J_{\text{tot}} = |J_{\phi}| + J_r + J_z$. The inner ($R_{\text{apo}} < 11$ kpc) and the outer ($R_{\text{apo}} > 15$ kpc) groups are squares and circles, respectively. Green and magenta solid lines in the bottom right-hand panel denote the regions of Gaia-Sausage/Enceladus (GSE; Belokurov et al. 2018; Helmi et al. 2018) and Sequoia (Barbá et al. 2019; Myeong et al. 2019), respectively. Grey small dots in the background of all panels are VMP stars studied in Sestito et al. (2020), in which the orbital parameters have been inferred with the same potential as this work.

of stars. The three panels on the left-hand side show the pericentric distance, the eccentricity, and the maximum height from the plane as a function of the apocentric distance. The right-hand two panels display the energy versus the rotational component of the action (top) and the action space (bottom). The sample appears to split into two broad populations in the Z_{\max} versus apocentre and the E versus J_{ϕ} panels – one that inhabits the inner region of the Milky Way ($R_{\text{apo}} \lesssim 10$ kpc) and one that reaches the outer part Milky Way halo ($R_{\text{apo}} \gtrsim 15$ kpc). We mark these with black squares and circles, respectively.

The first group is composed of four stars with apocentric distances of ~ 7 – 10 kpc. Three of them (LP3, LP4, and LP5) have pericentres that bring them into the spatial region of the Milky Way bulge ($R_{\text{peri}} < 3$ kpc). The remaining one, LP8, has a higher pericentre ($R_{\text{peri}} \sim 4.5$ kpc) and is among the lowest eccentricity stars in the sample ($\epsilon \sim 0.3$) – its $Z_{\max} < 3.0$ kpc and positive angular momentum indicate the

star is moving in a prograde orbit relatively close to the plane of the Milky Way. All stars in this group are prograde, with the exception of LP4, which has a very high eccentric orbit ($\epsilon \sim 0.7$), and almost no rotation ($J_{\phi}/J_{\text{tot}} \sim 0$). These EMP inner halo stars may be connected to very first Milky Way halo building blocks, the ancient Galactic disc and/or the chaotic (but slightly rotating) pre-disc Milky Way.

The second group is composed of the remaining seven stars with orbits compatible with outer halo stars. Three of them, LP1, LP9, and LP10, have pericentric distances in the range $2.0 < R_{\text{peri}} < 5.5$ kpc, the other four, LP2, LP6, LP7, and LP11, have larger pericentric distances. From the action space of Fig. 4, it is evident that none of our targets are clearly kinematically associated with GSE (green box) or Sequoia (magenta box). One of the stars, LP1 (sitting near the centre of the action diamond), could still have belonged to the GSE progenitor since it has high eccentricity (~ 0.75) and is not

far out of the GSE box. Previous works have associated some stars in this region with GSE (e.g. Yuan et al. 2020) or shown that in simulations there are GSE stars on a variety of orbits larger than the typical selection boxes (e.g. Naidu et al. 2021; Amarante et al. 2022). A possible association of LP11 (the most prograde star in the outer halo group) can be made with the Helmi stream (Helmi et al. 1999), as it sits in a similar region of the action diamond and the $E-J_\phi$ space (see e.g. Yuan et al. 2020) and has strong vertical motion ($J_z = 1084 \text{ kpc km s}^{-1}$), consistent with the very polar orbit of the Helmi stream. Association with other halo substructures (such as the dynamically tagged groups of VMP stars by Yuan et al. 2020 and others) is difficult due to the relatively large uncertainties on the orbital parameters for most stars. The majority of our stars were likely brought into the Milky Way in smaller accretion events.

High-resolution spectroscopic observations would be needed to determine the detailed chemo-dynamical properties of the stars in this work. They would provide better RVs to derive more precise orbital parameters and more importantly detailed chemical abundances, from different nucleosynthetic production channels, which are needed to better characterize the formation sites and origins of the stars in our sample.

4.2 CEMP stars

Following the Aoki et al. (2007) definition of CEMP stars ($[\text{C}/\text{Fe}] > +0.7$), three of our stars can be classified as carbon enhanced: LP1, LP6, and LP11. For two other objects (LP4 and LP9, with $T_{\text{eff}} \sim 6000 \text{ K}$ but no clear features within the G band), we were able to provide an informative upper limit of $[\text{C}/\text{Fe}] < +0.7$, making these carbon-normal stars. The other six targets (LP2, LP3, LP5, LP7, LP8, and LP10) are relatively warm ($T_{\text{eff}} > 6100 \text{ K}$) and the absence of CH absorption features only allows us to provide upper limits that are larger than $[\text{C}/\text{Fe}] = +0.7$, according to the sensitivity criteria from Aguado et al. (2019). We do not derive the fraction of CEMP stars in our sample, since the pre-selection was strongly biased.

Since we do not have estimates of any s-process element abundances for our sample,⁸ we cannot constrain the types of CEMP stars in our sample using that method. However, CEMP-s and CEMP-no stars also have different distributions in their metallicities and carbon abundances (e.g. Spite et al. 2013; Bonifacio et al. 2015; Yoon et al. 2016). We can use this to make a preliminary classification of CEMP stars. Fig. 5 presents the $[\text{Fe}/\text{H}]$ – $A(\text{C})$ ⁹ diagram of the stars in our sample, together with a compilation of CEMP stars from Yoon et al. (2016). The two most carbon-rich CEMP stars in our sample (LP6 and LP11) are on the border between the CEMP-no and CEMP-s regions. The third (LP1) lies in the CEMP-no region of the diagram, as well as the other stars with $[\text{C}/\text{Fe}]$ upper limits.

All three CEMP stars have large apocentres ($>20 \text{ kpc}$), and the two most carbon-rich CEMP stars also have the highest pericentres in our sample ($>8 \text{ kpc}$). As discussed above, these are indications that they likely came into the Milky Way in a relatively small dwarf galaxy. Previous work has suggested that the fraction of CEMP-no compared to CEMP-s stars are larger in the outer halo than in the inner halo (Yoon et al. 2018; Lee, Beers & Kim 2019), as well as in smaller halo building blocks (Yoon et al. 2019; Zepeda et al. 2022).

⁸There are two relatively strong lines of Sr and Ba in our wavelength coverage, but the combination of resolution, S/N, and extremely low metallicities of the stars do not permit their detection.

⁹ $A(\text{C}) = \log \epsilon(\text{C}) = \log (N_{\text{C}}/N_{\text{H}}) + 12$, with $A(\text{C})_{\odot} = 8.39$ from Asplund et al. (2005).

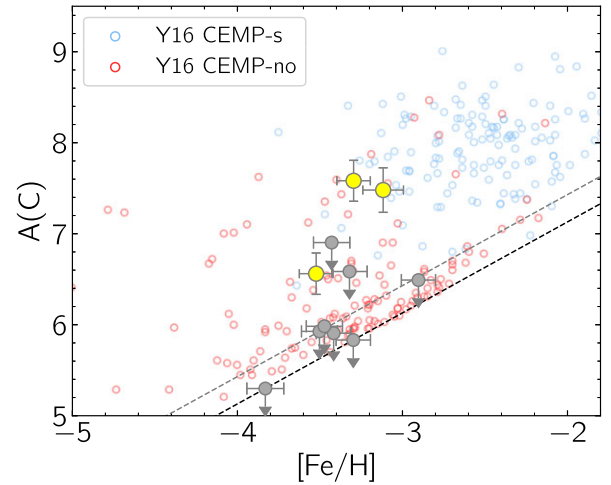


Figure 5. $[\text{Fe}/\text{H}]$ versus $A(\text{C})$ (corrected for evolutionary effects) for the stars in our sample (large yellow symbols, and grey symbols for upper limits) and the CEMP stars in the Yoon et al. (2016) compilation (small symbols colour coded by CEMP type). The uncertainties on $A(\text{C})$ are the quadratic sum of the adopted uncertainties on $[\text{Fe}/\text{H}]$ and $[\text{C}/\text{Fe}]$. The black and grey dashed lines indicate the limits of $[\text{C}/\text{Fe}] = +0.7$ and $+1.0$, respectively.

This is additional indirect evidence that the two most carbon-rich stars in our sample are more likely to be CEMP-no.

If LP6 and LP11 are CEMP-s stars, they are among the lowest metallicity CEMP-s stars known. If they are CEMP-no stars, they are among the highest $A(\text{C})$ CEMP-no stars known. There are not that many literature stars in this region, so it would be interesting to do further higher resolution follow-up of these two stars to investigate their nature.

4.3 LAMOST DR8 VaC comparison

A new analysis of the LAMOST DR8 spectra was published in a value-added catalogue (VaC) by Wang et al. (2022), employing neural networks to derive stellar parameters (T_{eff} , $\log g$, and $[\text{Fe}/\text{H}]$). They train one of the neural networks on stars of all metallicities in the PASTEL catalogue (Soubiran et al. 2010), and another network only on metal-poor stars ($[\text{Fe}/\text{H}] < -1.5$) to improve their $[\text{Fe}/\text{H}]$ estimates for VMP stars. They claim that the metallicities in their VMP catalogue are reliable down to $[\text{Fe}/\text{H}] \sim -3.5$.

10 out of our 11 OSIRIS stars have stellar parameters in the DR8 VaC (the only star absent is our most metal-rich star, LP8, with $[\text{Fe}/\text{H}]_{\text{FERRE}} = -2.9$). We present the comparison between the DR8 VaC metallicities and the metallicities derived in this work in Fig. 6. The very carbon-enhanced cool star LP6 has extreme metallicities in both the PASTEL and VMP catalogues, which is not unexpected since the spectrum is dominated by carbon features and this is not taken into account in the Wang et al. (2022) analysis. Focusing on the $[\text{Fe}/\text{H}]_{\text{VMP}}$ estimates, the other stars are all found to have systematically higher metallicities compared to our analysis, mostly in the range $-3.0 < [\text{Fe}/\text{H}]_{\text{W22}} < -2.3$. Since we are using spectra of much higher S/N and we are employing a dedicated analysis method for EMP (and/or carbon-enhanced) stars, we conclude that some caution should be taken with the Wang et al. (2022) VMP catalogues for $[\text{Fe}/\text{H}]_{\text{W22}} < -2.5$. We further note that more EMP stars may be hidden in large catalogues, especially among stars with low S/N spectra.

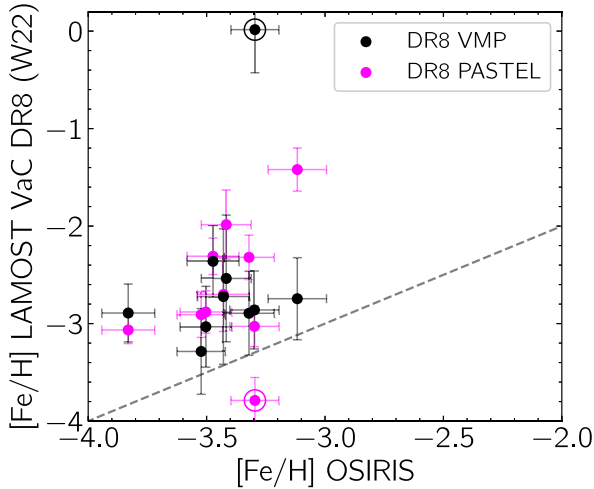


Figure 6. Comparison between our derived metallicities from the OSIRIS spectra and those from the Wang et al. (2022) LAMOST DR8 value-added catalogue. The points are colour coded by the version of the neural network applied to the DR8 data, and the cool CEMP star in our sample (LP6) has been highlighted with a large circle. The bisector is indicated with a grey dashed line.

5 SUMMARY

In this work, we employed the combination of metallicity-sensitive photometry from the *Pristine* survey (Starkenburg et al. 2017b) and the large low-resolution spectroscopic LAMOST data base to identify promising ultra-metal-poor and/or carbon-enhanced EMP candidates. We analysed ~ 7500 LAMOST spectra for targets with $[\text{Fe}/\text{H}]_{\text{Pristine}} < -2.5$ and $g < 18$, finding success rates of stars with $[\text{Fe}/\text{H}]_{\text{spec}} < -2.5$ between 34 per cent and 50 per cent, depending on the applied quality cuts. We inspected all the fits with $[\text{Fe}/\text{H}]_{\text{spec}} < -3.0$ to identify candidates for follow-up, and we release this full list together with figures of the best fits (see Section 2.3).

We observed 11 of the most exciting candidates (mostly with low LAMOST S/N) using OSIRIS at the GTC. We analysed the higher S/N medium-resolution OSIRIS spectra ($R \sim 2400$) using the FERRE code to derive T_{eff} , $[\text{Fe}/\text{H}]$, and $[\text{C}/\text{Fe}]$, adopting $\log g$ from photometry. The metallicities for the 11 stars range from $[\text{Fe}/\text{H}] = -2.9 \pm 0.1$ to -3.8 ± 0.2 , with a mean $[\text{Fe}/\text{H}] = -3.4$. We set out to identify ultra-metal-poor stars, but none of the targets had $[\text{Fe}/\text{H}] < -4.0$ – such stars are indeed incredibly rare. Our selection of (carbon-enhanced) EMP stars, however, was still very efficient.

For three out of the 11 stars we were able to derive carbon abundances, for the others we derived upper limits – two of which are constraining and classify the stars as carbon normal. Given their $[\text{Fe}/\text{H}]$, $A(\text{C})$, and orbital properties, all three CEMP stars are likely part of the CEMP-no category, although the two most carbon-rich objects lie in an underpopulated region, where there are both CEMP-no and CEMP-s stars in the literature. Further follow-up is necessary to understand the physical processes causing the carbon enhancement in these stars.

We derive orbital properties using the OSIRIS RVs, *Gaia* proper motions, and distances based on photometry and parallaxes from *Gaia* combined with MIST isochrones, integrating orbits in the MW POTENTIAL14 with a more massive halo. We find that four of the stars have inner halo kinematics, with three of them on prograde orbits. The other seven stars have orbits more consistent with the outer halo. None of the stars in our sample are confidently associated

with previously known substructures/accretion events, partly due to uncertainties on the orbital parameters.

Ongoing and upcoming spectroscopic surveys are so large that it is crucial to have general automatic analyses of the spectra, but doing this well for EMP stars is a challenge. They are only a small subset, hence pipelines are often not optimized for them, and their spectra are challenging to analyse due to weak spectral features and/or peculiar chemical abundances. It will remain important to do dedicated metal-poor analyses in the future. Adding additional information like metallicity-sensitive photometry as in this work could uncover hidden promising candidates at the lowest metallicities.

ACKNOWLEDGEMENTS

We thank the reviewer for their valuable comments, which helped improve the paper. The authors thank Carlos Allende Prieto, Carmela Lardo, and Lyudmila Mashonkina, as well as the rest of the *Pristine* Collaboration, for their support of this paper and/or their useful comments.

AA, NFM, and ZY gratefully acknowledge support from the European Research Council (ERC) under the European Union’s Horizon 2020 Framework Programme (grant agreement no. 834148). AA acknowledges support from the Herchel Smith Fellowship at the University of Cambridge and the Fitzwilliam College Isaac Newton Trust Research Fellowship. DSA acknowledges support from the European Research Council (ERC) Starting Grant NEFERTITI H2020/808240. FS thanks Dr Margaret ‘Marmie’ Perkins Hess post-doctoral fellowship for funding his work at the University of Victoria. JIGH acknowledges financial support from the Spanish Ministry of Science and Innovation (MICINN) project PID2020-117493GB-I00 and also from the Spanish MICINN under 2013 Ramón y Cajal program RYC-2013-14875. NFM and ZY acknowledge support from the French National Research Agency (ANR) funded project ‘*Pristine*’ (ANR-18-CE31-0017), NFM also acknowledges funding from INSU, CNRS through the Programme National Galaxies et Cosmologie and through the CNRS grant PICS07708. ES acknowledges funding through VIDI grant ‘Pushing Galactic Archaeology to its Limits’ (with project number VI.Vidi.193.093) that is funded by the Dutch Research Council (NWO). PJ acknowledges support from the Swiss National Science Foundation.

This study is based on observations made with the Gran Telescopio Canarias (GTC), installed at the Spanish Observatorio del Roque de los Muchachos of the Instituto de Astrofísica de Canarias, on the island of La Palma.

This study is also based on observations obtained with MegaPrime/MegaCam, a joint project of CFHT and CEA/DAPNIA, at the Canada–France–Hawaii Telescope (CFHT) that is operated by the National Research Council (NRC) of Canada, the Institut National des Sciences de l’Univers of the Centre National de la Recherche Scientifique of France, and the University of Hawaii.

Guoshoujing Telescope (the Large Sky Area Multi-Object Fibre Spectroscopic Telescope – LAMOST) is a National Major Scientific Project built by the Chinese Academy of Sciences. Funding for the project has been provided by the National Development and Reform Commission. LAMOST is operated and managed by the National Astronomical Observatories, Chinese Academy of Sciences.

Funding for the Sloan Digital Sky Survey IV has been provided by the Alfred P. Sloan Foundation, the U.S. Department of Energy Office of Science, and the Participating Institutions. SDSS-IV acknowledges support and resources from the Center for High Performance Computing at the University of Utah. The SDSS website is www.sdss.org. SDSS-IV is managed by the Astrophys-

ical Research Consortium for the Participating Institutions of the SDSS Collaboration including the Brazilian Participation Group, the Carnegie Institution for Science, Carnegie Mellon University, Center for Astrophysics | Harvard & Smithsonian, the Chilean Participation Group, the French Participation Group, Instituto de Astrofísica de Canarias, The Johns Hopkins University, Kavli Institute for the Physics and Mathematics of the Universe (IPMU)/University of Tokyo, the Korean Participation Group, Lawrence Berkeley National Laboratory, Leibniz Institut für Astrophysik Potsdam (AIP), Max-Planck-Institut für Astronomie (MPIA Heidelberg), Max-Planck-Institut für Astrophysik (MPA Garching), Max-Planck-Institut für Extraterrestrische Physik (MPE), National Astronomical Observatories of China, New Mexico State University, New York University, University of Notre Dame, Observatório Nacional/MCTI, The Ohio State University, Pennsylvania State University, Shanghai Astronomical Observatory, United Kingdom Participation Group, Universidad Nacional Autónoma de México, University of Arizona, University of Colorado Boulder, University of Oxford, University of Portsmouth, University of Utah, University of Virginia, University of Washington, University of Wisconsin, Vanderbilt University, and Yale University.

This work has made use of data from the European Space Agency (ESA) mission *Gaia* (<https://www.cosmos.esa.int/gaia>), processed by the *Gaia* Data Processing and Analysis Consortium (DPAC, <https://www.cosmos.esa.int/web/gaia/dpac/consortium>). Funding for the DPAC has been provided by national institutions, in particular the institutions participating in the *Gaia* Multilateral Agreement.

DATA AVAILABILITY

The LAMOST spectra used in this work are public. Our EMP candidate list is available in Table 1, and all relevant data for the OSIRIS stars are available in Tables 2–4. These tables will also be available at the CDS. The OSIRIS spectra will be shared on reasonable request to the authors.

REFERENCES

- Abohalima A., Frebel A., 2018, *ApJS*, 238, 36
- Aguado D. S., Allende Prieto C., González Hernández J. I., Carrera R., Rebolo R., Shetrone M., Lambert D. L., Fernández-Alvar E., 2016, *A&A*, 593, A10
- Aguado D. S., Allende Prieto C., González Hernández J. I., Rebolo R., Caffau E., 2017a, *A&A*, 604, A9
- Aguado D. S., González Hernández J. I., Allende Prieto C., Rebolo R., 2017b, *A&A*, 605, A40
- Aguado D. S., González Hernández J. I., Allende Prieto C., Rebolo R., 2018, *ApJ*, 852, L20
- Aguado D. S. et al., 2019, *MNRAS*, 490, 2241
- Allende Prieto C., Beers T. C., Wilhelm R., Newberg H. J., Rockosi C. M., Yanny B., Lee Y. S., 2006, *ApJ*, 636, 804
- Allende Prieto C. et al., 2015, *A&A*, 579, A98
- Amarante J. A. S., Debattista V. P., Beraldo E Silva L., Laporte C. F. P., Deg N., 2022, *ApJ*, 937, 12
- Anders F. et al., 2022, *A&A*, 658, A91
- Andrae R. et al., 2018, *A&A*, 616, A8
- Aoki W., Beers T. C., Christlieb N., Norris J. E., Ryan S. G., Tsangarides S., 2007, *ApJ*, 655, 492
- Arentsen A., Starkenburg E., Shetrone M. D., Venn K. A., Depagne É., McConnell A. W., 2019, *A&A*, 621, A108
- Arentsen A. et al., 2020, *MNRAS*, 491, L11
- Arentsen A. et al., 2021, *MNRAS*, 505, 1239
- Arentsen A., Placco V. M., Lee Y. S., Aguado D. S., Martin N. F., Starkenburg E., Yoon J., 2022, *MNRAS*, 515, 4082
- Asplund M., Grevesse N., Sauval A. J., 2005, in Barnes T. G., III, Bash F. N., eds, ASP Conf. Ser. Vol. 336, Cosmic Abundances as Records of Stellar Evolution and Nucleosynthesis in Honor of David L. Lambert. Astron. Soc. Pac., San Francisco, p. 25
- Bailer-Jones C. A. L., Rybizki J., Founesneau M., Mantelet G., Andrae R., 2018, *AJ*, 156, 58
- Bailer-Jones C. A. L., Rybizki J., Founesneau M., Demleitner M., Andrae R., 2021, *AJ*, 161, 147
- Barbá R. H., Minniti D., Geisler D., Alonso-García J., Hempel M., Monachesi A., Arias J. I., Gómez F. A., 2019, *ApJ*, 870, L24
- Beers T. C., Christlieb N., 2005, *ARA&A*, 43, 531
- Beers T. C., Preston G. W., Shectman S. A., 1985, *AJ*, 90, 2089
- Belokurov V., Kravtsov A., 2022, *MNRAS*, 514, 689
- Belokurov V., Erkal D., Evans N. W., Koposov S. E., Deason A. J., 2018, *MNRAS*, 478, 611
- Belokurov V., Sanders J. L., Fattahi A., Smith M. C., Deason A. J., Evans N. W., Grand R. J. J., 2020, *MNRAS*, 494, 3880
- Bland-Hawthorn J., Gerhard O., 2016, *ARA&A*, 54, 529
- Boender C. G. E., Rinnoy Kan A. H. G., Timmer G. T., Stougie L., 1982, *Math. Programming*, 22, 125
- Bonaca A., Conroy C., Wetzel A., Hopkins P. F., Kereš D., 2017, *ApJ*, 845, 101
- Bonifacio P. et al., 2015, *A&A*, 579, A28
- Bovy J., 2015, *ApJS*, 216, 29
- Buder S. et al., 2021, *MNRAS*, 506, 150
- Caffau E. et al., 2013, *A&A*, 560, A71
- Carter C. et al., 2021, *ApJ*, 908, 208
- Cepa J. et al., 2000, in Iye M., Moorwood A. F., eds, Proc. SPIE Vol. 4008, Optical and IR Telescope Instrumentation and Detectors. SPIE, Bellingham, p. 623
- Choi J., Dotter A., Conroy C., Cantiello M., Paxton B., Johnson B. D., 2016, *ApJ*, 823, 102
- Christlieb N., Schörrck T., Frebel A., Beers T. C., Wisotzki L., Reimers D., 2008, *A&A*, 484, 721
- Conroy C. et al., 2022, preprint ([arXiv:2204.02989](https://arxiv.org/abs/2204.02989))
- Cordoni G. et al., 2021, *MNRAS*, 503, 2539
- Da Costa G. S. et al., 2019, *MNRAS*, 489, 5900
- Da Costa G. S., Bessell M. S., Nordlander T., Hughes A. C. N., Mackey A. D., Spitler L. R., Zucker D. B., 2022, preprint ([arXiv:2210.05161](https://arxiv.org/abs/2210.05161))
- Deng L.-C. et al., 2012, *Res. Astron. Astrophys.*, 12, 735
- Di Matteo P., Haywood M., Lehnert M. D., Katz D., Khoperskov S., Snaith O. N., Gómez A., Robichon N., 2019, *A&A*, 632, A4
- Di Matteo P., Spite M., Haywood M., Bonifacio P., Gómez A., Spite F., Caffau E., 2020, *A&A*, 636, A115
- Dotter A., 2016, *ApJS*, 222, 8
- El-Badry K. et al., 2018, *MNRAS*, 480, 652
- Falcón-Barroso J., Sánchez-Blázquez P., Vazdekis A., Ricciardelli E., Cardiel N., Cenarro A. J., Gorgas J., Peletier R. F., 2011, *A&A*, 532, A95
- Fernández-Alvar E. et al., 2021, *MNRAS*, 508, 1509
- Frebel A., Norris J. E., 2015, *ARA&A*, 53, 631
- Galarza C. A. et al., 2022, *A&A*, 657, A35
- Gallart C., Bernard E. J., Brook C. B., Ruiz-Lara T., Cassisi S., Hill V., Monelli M., 2019, *Nat. Astron.*, 3, 932
- Gratton R. G., Sneden C., Carretta E., Bragaglia A., 2000, *A&A*, 354, 169
- Green G. M., Schlafly E., Zucker C., Speagle J. S., Finkbeiner D., 2019, *ApJ*, 887, 93
- Hansen T. T., Andersen J., Nordström B., Beers T. C., Placco V. M., Yoon J., Buchhave L. A., 2016a, *A&A*, 586, A160
- Hansen T. T., Andersen J., Nordström B., Beers T. C., Placco V. M., Yoon J., Buchhave L. A., 2016b, *A&A*, 588, A3
- Haywood M., Di Matteo P., Lehnert M. D., Snaith O., Khoperskov S., Gómez A., 2018, *ApJ*, 863, 113
- Helmi A., White S. D. M., de Zeeuw P. T., Zhao H., 1999, *Nature*, 402, 53
- Helmi A., Babusiaux C., Koppelman H. H., Massari D., Veljanoski J., Brown A. G. A., 2018, *Nature*, 563, 85
- Howes L. M. et al., 2014, *MNRAS*, 445, 4241
- Howes L. M. et al., 2015, *Nature*, 527, 484

- Howes L. M. et al., 2016, *MNRAS*, 460, 884
- Hughes A. C. N. et al., 2022, *ApJ*, 930, 47
- Ibata R. A., Gilmore G., Irwin M. J., 1994, *Nature*, 370, 194
- Ibata R. et al., 2021, *ApJ*, 914, 123
- Koesterke L., Allende Prieto C., Lambert D. L., 2008, *ApJ*, 680, 764
- Koleva M., Prugniel P., Bouchard A., Wu Y., 2009, *A&A*, 501, 1269
- Koppelman H. H., Helmi A., Massari D., Price-Whelan A. M., Starkenburg T. K., 2019, *A&A*, 631, L9
- Lee Y. S. et al., 2013, *AJ*, 146, 132
- Lee Y. S., Beers T. C., Kim Y. K., 2019, *ApJ*, 885, 102
- Li H., Tan K., Zhao G., 2018, *ApJS*, 238, 16
- Li T. S. et al., 2022, *ApJ*, 928, 30
- Lindgren L. et al., 2021, *A&A*, 649, A2
- Lucey M. et al., 2022, *MNRAS*, 509, 122
- Martin N. F. et al., 2022a, *MNRAS*, 516, 5331
- Martin N. F. et al., 2022b, *Nature*, 601, 45
- Matijević G. et al., 2017, *A&A*, 603, A19
- Miyamoto M., Nagai R., 1975, *PASJ*, 27, 533
- Myeong G. C., Vasiliev E., Iorio G., Evans N. W., Belokurov V., 2019, *MNRAS*, 488, 1235
- Naidu R. P. et al., 2021, *ApJ*, 923, 92
- Navarro J. F., Frenk C. S., White S. D. M., 1997, *ApJ*, 490, 493
- Placco V. M., Frebel A., Beers T. C., Stancliffe R. J., 2014, *ApJ*, 797, 21
- Placco V. M., Beers T. C., Reggiani H., Meléndez J., 2016, *ApJ*, 829, L24
- Placco V. M. et al., 2018, *AJ*, 155, 256
- Placco V. M., Almeida-Fernandes F., Arentsen A., Lee Y. S., Schoenell W., Ribeiro T., Kanaan A., 2022, *ApJS*, 262, 8
- Prugniel P., Soubiran C., 2001, *A&A*, 369, 1048
- Prugniel P., Vauglin I., Koleva M., 2011, *A&A*, 531, A165
- Rix H.-W. et al., 2022, *ApJ*, 941, 45
- Ryan S. G., Norris J. E., 1991, *AJ*, 101, 1835
- Sánchez-Blázquez P. et al., 2006, *MNRAS*, 371, 703
- Sbordone L., Bonifacio P., Castelli F., 2007, in Kupka F., Roxburgh I., Chan K. L., eds, *Proc. IAU Symp. 239, Convection in Astrophysics*. Cambridge Univ. Press, Cambridge, p. 71
- Schiavon R. P. et al., 2017, *MNRAS*, 466, 1010
- Schlafman K. C., Casey A. R., 2014, *ApJ*, 797, 13
- Sestito F. et al., 2019, *MNRAS*, 484, 2166
- Sestito F. et al., 2020, *MNRAS*, 497, L7
- Sestito F. et al., 2021, *MNRAS*, 500, 3750
- Sestito F. et al., 2023, *MNRAS*, 518, 4557
- Sharma K., Prugniel P., Singh H. P., 2016, *A&A*, 585, A64
- Soubiran C., Le Campion J. F., Cayrel de Strobel G., Caillo A., 2010, *A&A*, 515, A111
- Spite M., Caffau E., Bonifacio P., Spite F., Ludwig H. G., Plez B., Christlieb N., 2013, *A&A*, 552, A107
- Starkenburg E., Oman K. A., Navarro J. F., Crain R. A., Fattahi A., Frenk C. S., Sawala T., Schaye J., 2017a, *MNRAS*, 465, 2212
- Starkenburg E. et al., 2017b, *MNRAS*, 471, 2587
- Steinmetz M. et al., 2006, *AJ*, 132, 1645
- Venn K. A. et al., 2020, *MNRAS*, 492, 3241
- Wang C., Huang Y., Yuan H., Zhang H., Xiang M., Liu X., 2022, *ApJS*, 259, 51
- Wu Y., Singh H. P., Prugniel P., Gupta R., Koleva M., 2011, *A&A*, 525, A71
- Wu Y., Du B., Luo A., Zhao Y., Yuan H., 2014, in Heavens A., Starck J.-L., Krone-Martins A., eds, *Proc. IAU Symp. 306, Statistical Challenges in 21st Century Cosmology*. Cambridge Univ. Press, Cambridge, p. 340
- Yong D. et al., 2013, *ApJ*, 762, 27
- Yoon J. et al., 2016, *ApJ*, 833, 20
- Yoon J. et al., 2018, *ApJ*, 861, 146
- Yoon J., Beers T. C., Tian D., Whitten D. D., 2019, *ApJ*, 878, 97
- York D. G. et al., 2000, *AJ*, 120, 1579
- Youakim K. et al., 2017, *MNRAS*, 472, 2963
- Yuan Z. et al., 2020, *ApJ*, 891, 39
- Zepeda J. et al., 2022, preprint ([arXiv:2209.12224](https://arxiv.org/abs/2209.12224))

SUPPORTING INFORMATION

Supplementary data are available at *MNRAS* online.

Table 1. List of 481 EMP candidates (533 spectra) with FERRE spectroscopic parameters used for target selection. Figures for the spectral fits of each of the entries in Table 1 are available in the supplementary data as well.

Please note: Oxford University Press is not responsible for the content or functionality of any supporting materials supplied by the authors. Any queries (other than missing material) should be directed to the corresponding author for the article.

This paper has been typeset from a \LaTeX file prepared by the author.